EUROFUSION WPDTT1-PR(14) 12746

G Calabro et al.

EAST Alternative Magnetic Configurations: Modelling and First Experiments

Preprint of Paper to be submitted for publication in Nuclear Fusion

This work has been carried out within the framework of the EUROfusion Consortium and has received funding from the Euratom research and training programme 2014-2018 under grant agreement No 633053. The views and opinions expressed herein do not necessarily reflect those of the European Commission.

EAST Alternative Magnetic Configurations: Modelling and First Experiments

G. Calabrò[1], B.J. Xiao[2,3], S. L. Chen[2], Y.M. Duan[2], Y. Gong[2], J.G. Li[2], Z.P. Luo[2], L. Wang[2], J. Xu[2], B. Zhang[2], R. Albanese[4], R. Ambrosino[4], F. Crisanti[1], V. Pericoli Ridolfini[4], F. Villone[4], B. Viola[1], L. Barbato[4], M. De Magistris, [4], G. De Tommasi[4], E. Giovannozzi[1], S. Mastrostefano[4], S. Minucci[4], A. Pironti[4], G. Ramogida[1], A.A. Tuccillo[1], R. Zagórski[5] and EAST team[*]

[1]ENEA for EUROfusion, via E. Fermi 45, 00044 Frascati (Rome), Italy
[2]Institute of Plasma Physics, Chinese Academy of Sciences, Hefei, 230031, China
[3]School of Nuclear Science and Technology, University of Science and Technology of China, Hefei, 230026, China
[4]CREATE, Università di Napoli Federico II, Università di Cassino and Università di Napoli Parthenope, Via Claudio 19, 80125 Napoli, Italy
[5]Institute of Plasma Physics and Laser Microfusion, Warsaw, Poland

E-mail contact of main author: giuseppe.calabro@enea.it

Abstract. Heat and particle loads on the plasma facing components are among the most challenging issues to be solved for a reactor design. Alternative magnetic configurations, such as the X-divertor (X-d), Super X-divertor and Snowflake (SF) divertor may enable tokamak operation with a lower peak heat load than a standard Single Null (SN) divertor. This paper reports on the modelling of the variations of the second null point present in the alternative magnetic divertors to span the spectrum from X-d to SF like configuration (or SF to X-d) on EAST tokamak. Preliminary experiment with the second null forming a configuration with significant distance between the two nulls and a flaring geometry near the target plates have been performed in 2014. These configurations have been designed using the FIXFREE code and optimized with CREATE-NL tools and are discussed in the paper. Predictive edge simulations using the TECXY code are also presented by comparing the advanced divertor and SN configuration. Finally, the experimental results of ohmic and low confinement (L-mode) alternative divertor and SN discharges and interpretative 2D edge simulations are discussed. Future experiments will be devoted to vary the distance between the two nulls moving from a flaring to a contracting geometry near the target plates.

1. Introduction

Heat and particle loads on the plasma facing components are among the most challenging issues to be solved for a reactor design [1, 2]. One approach to handling the high exaust power is to use alternative magnetic configurations, such as the X-divertor (X-d) [3], Super X-divertor [4] and Snowflake Divertor (SF) [5]. The X-divertor places a second x-point near the plate, causing flared field lines there, which spreads the heat over a larger area and increases the line connection length both near the plate. The SF configuration is characterized by a second-order null (x-point) in the poloidal magnetic field (Bp), where both Bp itself and its spatial derivatives vanish ($B_p = 0$, $\nabla B_p = 0$). This splits the separatrix near the null into six segments: two enclose the confined plasma and four lead to the machine wall (the divertor legs). The poloidal cross-section of the obtained magnetic flux surfaces with a hexagonal null-point has the appearance of a snowflake. Theoretical studies indicate that the SF magnetic geometry may lead to both higher power losses during scrape-off layer (SOL) transport and an increased plasma wetted area of the wall [6, 7]. The former results from an increase in the connection length and the divertor volume, the latter from an increase in flux expansion and SOL width. The SF was first established on TCV [8], and later on the spherical tokamak

[*] See the appendix of B. Wan et al., Proceedings of the 25th IAEA Fusion Energy Conf., S. Petersburg, Russian Federation (2014) OV/3-3

NSTX [9] and finally in the larger tokamak DIII-D [10]. First experiments on the Experimental Advanced Superconducting Tokamak (EAST) in 2014 have been motivated from the goal to test the promises/potential of alternative magnetic divertors by spannig the spectrum from X-d like to SF like configuration (or SF to X-d). In the past, similar divertor studies have been conducted on TCV and discussed here [11]. As shown in Fig. 1, EAST is constructed to be up-down symmetric, with the following main parameters [12]: major radius R = 1.8 m, minor radius a = 0.45 m, toroidal field B_T up to 3.5 T, and plasma current I_p up to 1 MA for highly elongated plasmas with an elongation κ = 1.9. It can be operated in quite flexible plasma shapes with an elongation factor κ = 1.5-2.0 and triangularity δ = 0.3-0.6 for double null (DN) or SN divertor configurations. EAST is equipped with 14 superconducting Poloidal Field Coils for ohmic heating, ohmic current drive, shaping and position control [13] located outside the toroidal field coils (TFCs).

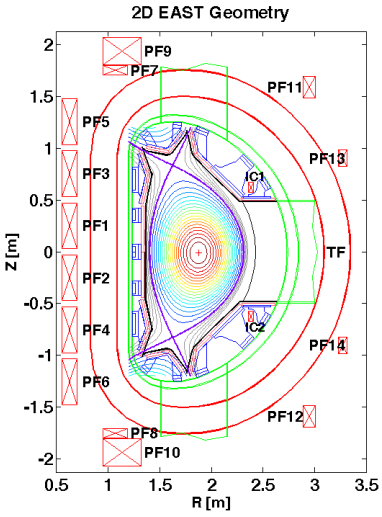

Figure 1. Two-dimensional EAST geometry schematic view.

It should be noted that PFCs 7 and 9 are connected in series as are PFCs 8 and 10. Thus, there are in total 12 independent PF power supplies (maximum current I_{PF} = 14.5kA). EAST also has in-vessel active feedback coils (IC coils) for fast control of the plasma vertical instability; they consist of two 2-turn coils symmetrically located in the upper and lower part of the vessel and connected in anti-series in order to provide an horizontal field. Unlike DIII-D and NSTX, EAST does not have dedicated divertor coils which could be used to shape the local flux distribution within the divertor region. In addition, EAST have only 12 independent PFCs to form SF configuration, for instance considerable fewer than in TCV, that presently is the most flexible machine to realize SF configuration. Before presenting the EAST alternative magnetic divertor studies and experimental results, it should be considered that the exact SF constitutes a single null point in the magnetic configurations space. As was realized in the first assessment of the SF [5] that an exact snowflake configuration is topologically unstable. Any variation of the PF coil currents, either by choice and/or pertubations of the magnetic equilibrium caused e.g. by plasma instabilities, splits the second-order null in two first-order nulls (x_1, x_2).

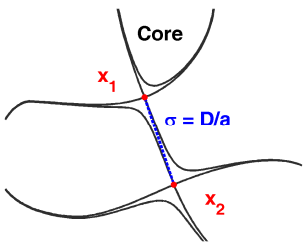

Figure 2. Schematic of variation in SF configuration, indicating the primary and the secondary x-points (x_1, x_2) and the dimensionaless SF proximity parameter σ = D/a.

As shown in Fig. 2, both x-points have an associated separatrix, with the one defining the last closed flux-surface (LCFS), called primary, and the other secondary. The distance between the two x-points, i.e. the proximity to the exact SF [14], is parametrized by the dimensionless parameter σ=D/a, with D the x-points separation and a the plasma minor radius. The position of x_2 relative to x_1 determines the local geometry of the null region and hence the properties of the divertor. There are two classes of SF configurations: (i) in the SF+, all SOL fieldlines

connect to primary SPs, as x_2 resides in the private flux region (see Fig. 2); (ii) in the SF−, one of the secondary SPs is connected by fieldlines to the SOL, as x_2 resides in the SOL (not shown here). Systematic assessments of the proximity condition to exact SF in terms of exaust properties are well described in [14, 15]. It should be noted that in EAST, due to the location of PF coils and target plates, as will be discussed in the next section, the secondary x-point could be moved around from the primary one to form a magnetic configuration that features the SF+ (or SF-), characterized by a contracting geometry near the plate [5], or an X-d configuration, characterized by a flaring geometry near the plate [16, 17]. In the rest of the paper, we shall refer to the configurations with the two x-points affecting the divertor geometry as quasi-SF (QSF) configurations indicating for each configuration the features of SF or X-d. The paper is organized as follows. Section 2 describes the QSF equilibrium configurations design and optimization, taking into account the technological constraints of the EAST tokamak. In Section 3 edge predictive simulations by comparing SN and QSF configurations will be given. Section 4 describes first ohmic and low confinment (L-mode) quasi-snowflake experiments in EAST and preliminary interpretative 2D edge simulations. Finally, Section 5 contains a summary and an outlook.

2. EAST QSF equilibria modelling and optimization

QSF configurations have been designed and optimized by means of CREATE-NL code (non linear plasma evolution code), described in [18], in combination with the EFIT [19] and FIXFREE [20] static equilibrium codes. The tokamak simulation code (TSC) [21], a numerical model of the axisymmetric tokamak plasma and the associated control systems, has been then used to model the EAST QSF full plasma time evolution scenario. The procedure proposed for the design and optimization of QSF configurations using the CREATE-NL code exploits the linearized relation between the plasma-wall gaps and the PF currents, as discussed in [22]. It is composed of two steps:

i) the first step allows to have a first cut of the QSF equilibrium starting from a standard single null plasma configuration: a new equilibrium with a second null point within a limited distance from the SN x-point is obtained, forcing the plasma boundary to be almost unchanged, apart from the region in the vicinity of the null point;

ii) the second step refines the plasma shape and possibly reduces the PF coil currents while fulfilling the machine technological constraints. Recently, the same technique has been successfully used on TCV in order to optimize experimental SF configurations [23].

Here, QSF equilibria are identified as modifications of the EAST SN discharge #43362 (I_P ~ 400kA, B_T = 1.8T, internal plasma inductance l_i ~1.4, poloidal beta β_p~0.1) with the following constraints to be verified:

a) PF coil currents I_k far enough from their limits: $I_{min} + \Delta I \leq I_k \leq I_{max} - \Delta I$, with $\Delta I = 0.1 \max\{|I_{min}|, |I_{max}|\}$;

b) vertical instability growth rate not much larger than reference SN configuration;

c) strike points on vertical targets;

d) at least 40 mm clearance (gap) between plasma boundary and first wall.

The objectives of the QSF design and optimization procedure consists in the definition of a set of QSF equilibria, at low (0.1) and high β_p (0.45) with the secondary x-point close or far from the vessel structures maximizing the plasma current.

The vertical stability analyses have been carried out using the passive structures in their configuration before the changes made in 2014, assuming that with the new configuration, EAST can operate at least with plasmas having similar growth rates. A detailed comparison of model predictions with the experimentally measured growth rates of VDEs has been carried out for several configurations, ranging from low (<100s^{-1}), to medium (around 200s^{-1}) up to high (>300s^{-1}) values [24]. CREATE_L (linearized axisymmetric model) [25] and CarMa0 (linearized model with 3D conducting structure and axisymmetric plasma) [26] have been used for this study.

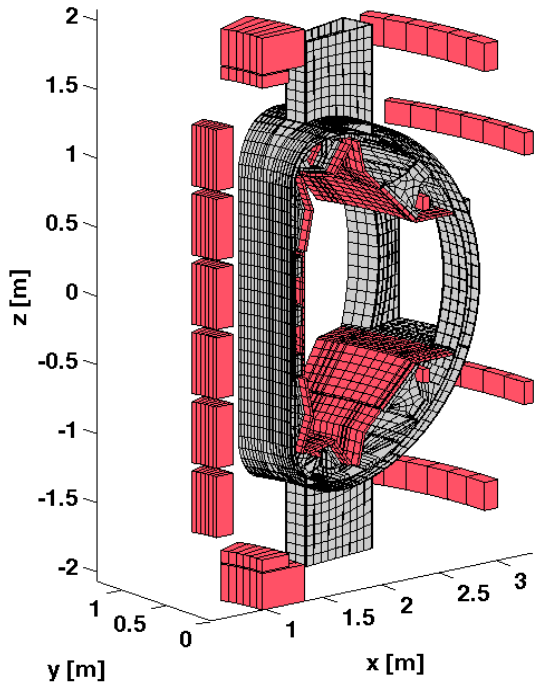

Figure 3. Details of the 3D structure used for vertical stability analyses.

Different axisymmetric models have been computed, with the following assumptions on conducting structures (all structures are assumed as toroidally continuous with nominal resistivity):

a) vessel only;

b) vessel + passive plates (PP);

c) vessel + passive plates (PP) + all plasma facing components.

Assumption a) leads always to plasmas which are unstable on the Alfvén time scale (the vessel is "too far" from the plasma to provide effective stabilization). Assumption c) provides a lower bound for the actual growth rate, since PP and plasma facing components are not toroidally continuous, but are connected to the vessel through suitable supports. Conversely, assumption b) provides an upper bound to growth rate, since the plasma facing components do provide some stabilizing effect. The 3D model instead self-consistently take into account the actual geometry of the conducting structures. Fig. 3 shows some details of the 3D structure used for vertical stability analyses.

The optimized QSF configurations obtained with CREATE-NL and then verified by EFIT and FIXFREE code are summarized in Table I. The growth rates of the QSF configurations are reasonably close to those of previous EAST experiments [24]. The low β_p "close nulls" option provides a somewhat more challenging value of the growth rate, which is probably related to the lower stability margin of this configuration. Also typical geometrical factors as connection length L and polodal magnetic flux expansion f_m [14] in the outer SP region, and the x-point separation D for the optimized QSF equilibria are reported. The connection length is evaluated averaging over an outboard equatorial depth of 2mm. The simulated QSF and experimental reference SN equilibria at low β_p are shown in Fig. 4. It should be noted that for the QSF configurations with I_P=400 kA the secondary x-point is located on the vessel (on the inner shell at low β_p, on the outer shell location for a high β_p case, not shown here). However, the secondary x-point point may be brought inside the vessel at the price of a slightly lower plasma current or a higher plasma elongation and/or a futher optmization of the PF coil

currents. In addition, the "close nulls" QSF equilibria present higher flux expansion at the divertor plates. Finally, the high β_p configurations are slightly more demanding in terms of PF currents and present larger x-points separation D.

Table I. EAST optimized QSF configurations by CREATE-NL code

	QSF low β_p 400kA "close nulls"	**QSF high β_p 400kA "close nulls"**	**QSF low β_p 480kA "far nulls"**	**QSF high β_p 480kA "far nulls"**	**Reference SN 43362**
I_P [kA]	400	400	480	480	388
β_p	0.1	0.45	0.1	0.45	0.1
l_i	1.4	1.4	1.4	1.4	1.26
IPF1 [A]	2560	3789	3366	6897	-196
IPF2 [A]	-13050	-13051	-13016	-13027	-203
IPF3 [A]	9407	9513	6635	4319	222
IPF4 [A]	2707	2028	2050	306	-1432
IPF5 [A]	-9398	-12706	-7363	-10229	2158
IPF6 [A]	13050	13051	13016	13027	3956
IPF7_9 [A]	1198	2649	2222	4020	5233
IPF8_10 [A]	-970	-742	218	566	5282
IPF11 [A]	5322	4368	4033	2769	-6055
IPF12 [A]	7145	6779	5557	5255	-5981
IPF13 [A]	-13050	-13051	-13016	-13027	-192
IPF14 [A]	-13050	-13051	-13016	-13027	-622
IC [A]	0	0	0	0	0
max(abs(currents)) [A]	13050	13051	13016	13027	6055
x-points separation D (cm) (only for QSF cases)	39	45	84	92	-
κ	1.73	1.72	1.71	1.71	1.65
Volume [m^3]	12.21	12.59	12.28	12.76	11.02
Flux Expansion f_m	26.59	22.29	9.84	11.09	2.09
Connection length L (m)	129.74	126.23	103.50	101.47	94.93
Growth rate lower bound [s^{-1}]	186	161	148	120	88
Growth rate upper bound [s^{-1}]	474	339	341	241	195
Growth rate with 3D mesh of old struture [s^{-1}]	454	312	258	198	120
Stability margin with 3D mesh of old structure	0.23	0.31	0.35	0.44	0.61

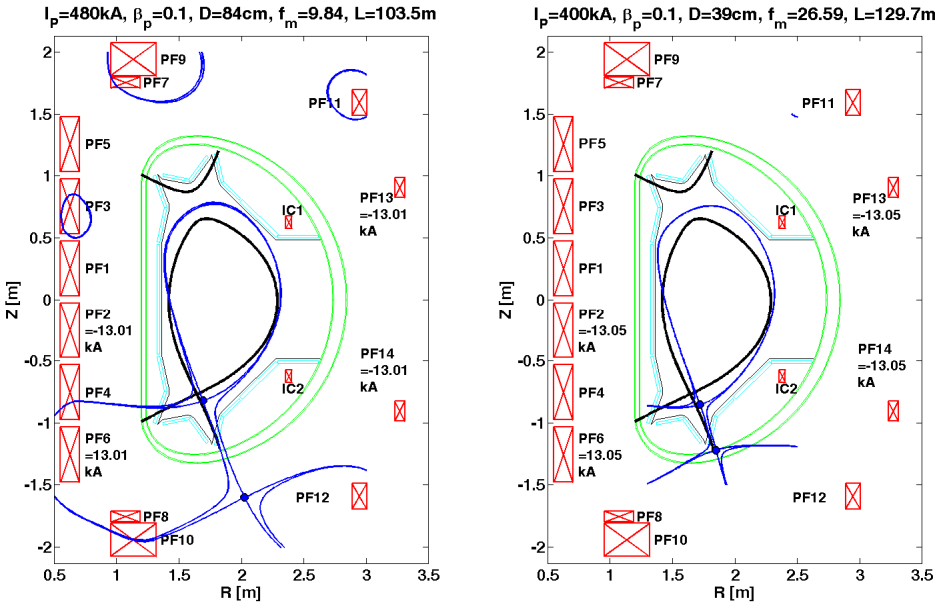

Figure 4. Plasma boundary of optimized QSF (blue solid line) and reference SN equilibria (black solid line), at low β_p, calculated by CREATE-NL code. Also the x-point separation D, the connection length L, the polodal magnetic flux expansion f_m in outer SP region and maximum obtained PF currents are reported for QSF equilibria. For the SN configuration: L=95m, f_m=2.1.

3. Edge predictive simulations

Predictive edge simulations of standard SN divertor and QSF configuration, here the "far null case" presented in section 3, have mainly been run with the flexible, quick and versatile multifluid 2D edge code TECXY [27]. TECXY takes into account all the main physics processes, atomic and plasma, occurring in the SOL, but the neutral dynamics, i.e. generation of atoms at the solid surfaces and transport into the SOL, is treated with an analytical model instead of the more rigorous Monte Carlo method. In addition, in TECXY the divertor plates are always assumed to be perpendicular to the flux surfaces, as discussed in [27]. The plasma status when it is detached from the divertor target cannot be reliably modelled, but only the approach to such conditions can be outlined. The parameters considered in the simulations have been: outboard density at separatrix $1.5 \leq n_{e,sep} \leq 4.2\times10^{19}$ m^{-3}, corresponding roughly to the line averaged density range 3.5-10 $\times10^{19}$ m^{-3}, power input into the SOL P_{SOL} = 3MW, I_P = 300kA and B_T = 1.8T. In this studies, the e-folding length power decay λ of 1cm has been assumed for EAST, according to the studies presented in [28]. No impurity has been considered. In Fig.5 the total power deposited on both (inner and outer) divertor plates for SN and QSF is shown versus the plasma density at the outboard midplane. The QSF curve is always below the SN one, i.e. the total volume losses are higher. As already found in the code runs for the tokamak proposal FAST [29] the load mitigating properties of the QSF are exalted at higher density. Indeed, a further significant drop for the QSF total load is found for $n_{e,sep} \geq 2.5\times10^{19}$ m^{-3} in EAST. According to the previous studies the main physics mechanism responsible for the higher QSF volume losses could be due to the longer magnetic connection length inside the divertor region. This prolongs the particle dwell time inside the SOL so that the number of interaction with the background neutrals during the particle lifetime increases and the energy losses are enhanced. In parallel to the divergence of the two curves, the features of plasma detachment are expected to appear. Indeed just at that value of $n_{e,sep}$, the peak power load on the outer target for SN and QSF (see Fig.6.) shows a clear change in the

slope for QSF with a saturation at vary low value, which is a sign of an efficient shielding of the plate. No significant change is instead observed for SN, whose values are divided by 10 in the figure for facilitating the comparison. It has to be noted for the sake of clarity that these loads correspond to targets perpendicular to the poloidal field: the actual values should take into account the real inclination of the plates.

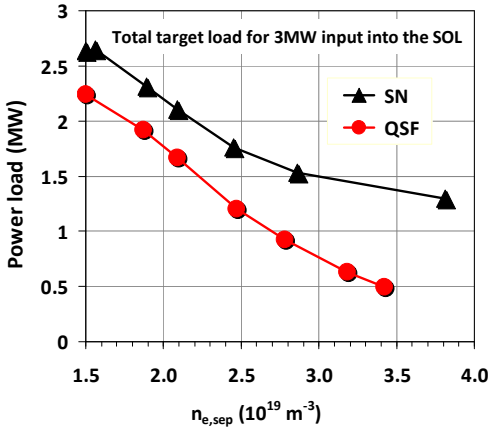

Figure 5. Total load on both targets versus the plasma density at the outboard midplane. The power input into the SOL is 3.0 MW.

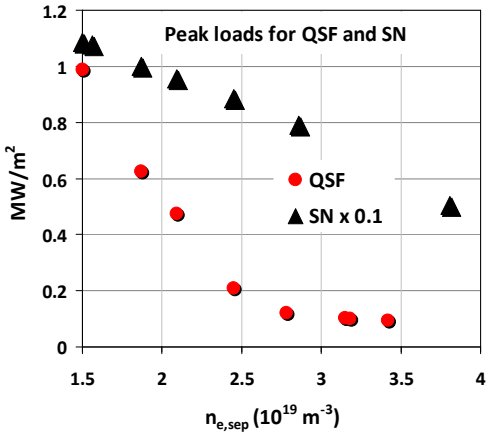

Figure 6. Peak power load onto the outer target versus the plasma density at the outboard midplane for both standard (SN) and quasi snow flake (QSF) divertor.

Validation to these results comes from the case so far considered also with EDGE2D code [30], where the actual divertor geometry is considered and the neutrals dynamics is treated with a Monte Carlo computing technique. This is shown in Fig.7 where the ratio (SN over QSF) between the peak values of the loads onto the outer target versus the density at separatrix on the outboard equator is shown.

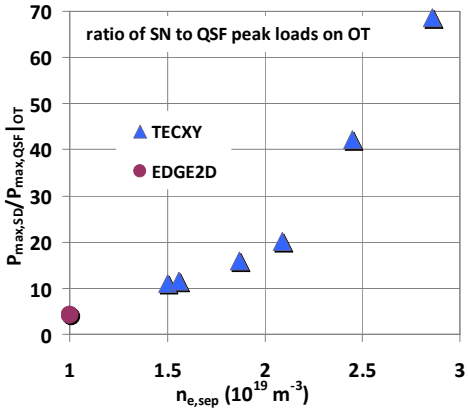

Figure 7. QSF peak mitigation factor, as derived from TECXY and EDGE2D runs. The point from this last code aligns very well to the others, despite the very different calculation method.

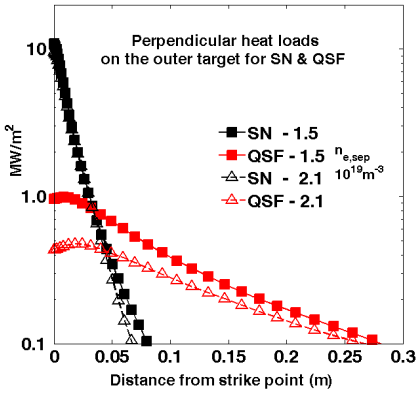

Figure 8. Power deposition profiles on to the outer target for two densities at separatrix for QSF (in red) and SN (in black). The target is set perpendicular to the poloidal field in the simulation.

The point at the lowest density, derived from EDGE2D, is clearly the prolongation of the curve obtained from TECXY runs. This figure also clearly shows how strong the mitigation of the peak deposition power can be, as combination of the flux expansion, which dominates at low density, and of the enhanced dissipation processes, which dominate at the higher densities. Again the slope chages close to $n_{e,sep} = 2.5\times10^{19}$ m^{-3} should be attributed to the onset of detachment. The deposition profiles on the outer divertor target, with $n_{e,sep}$ = 1.5 and

2.1×10^{19} m^{-3}, are finally presented in Fig. 8. For the higher density this figure not only details for QSF the large improved mitigation of the peak power, but also clearly puts into evidence how the load smears out over a longer distance and the peak position is slightly outwards shifted. Neither of the two last features is present in the SN curves. The second one (i.e. the peak shift) is the first hint of detachment. In summary, the predictive work with TECXY and EDGE2D indicates that a benefit, in terms of power load onto the divertor, is expected from changing the divertor magnetic configuration form the standard to the QSF configuration. In addition, the mitigation apparently improves at the highest densities, as found in other papers, and should be particularly evident with high additional heating power, since a stronger absolute drop of the loads has to develop for the same mitigation factor.

4. Experimental results

First QSF experiments have been performed on EAST in 2014, after nearly 20-month-long upgrading break. The major upgrades [31] include: Heating and Current Drive (H&CD) systems increase to 26MW from 10MW, including a 4MW (50-80keV) of Neutral Beam Injection (NBI) system, new 76 different diagostics installed and the upper divertor changed into ITER-like actively cooled W monoblock configuration with up to 10MW/m^2 heat removing capacity (where the lower divertor has been kept in Carbon material with Molybdenom-tiled vacuum vessel). In these experiments the simplest form of plasma current and position (i.e. plasma centroid) control has been used, the so-called RZIP control [32]. The control parameters are regulated by adjusting the current in the PF coils. The requested PF coil current is composed of the sum of feed-forward (FF) and feedback (FB) components. The adaptation of the more sophisticated EAST ISOFLUX shape controller [13] to QSF configuration is still on-going and it will be implemented during the next experimental campaign. The PFC currents discussed in section 2 have been used as FF component target in RZIP control for QSF experiments (here only “far nulls” case). Magnetic and plasma characteristics of QSF have been studied in discharges with I_P=250kA and B_T=1.8T, κ~1.9, q_{95}~8, ohmic and with ~500kW of NBI heating. It should be noted that the plasma current in these first QSF experiments has been purposely kept low for safety reasons. Fig. 9. shows the experimental magnetic equilibri, reconstructed with the Grad-Shafranov equilibrium code EFIT using standard magnetic constraints [19] at different times of the ohmic discharge #47660.

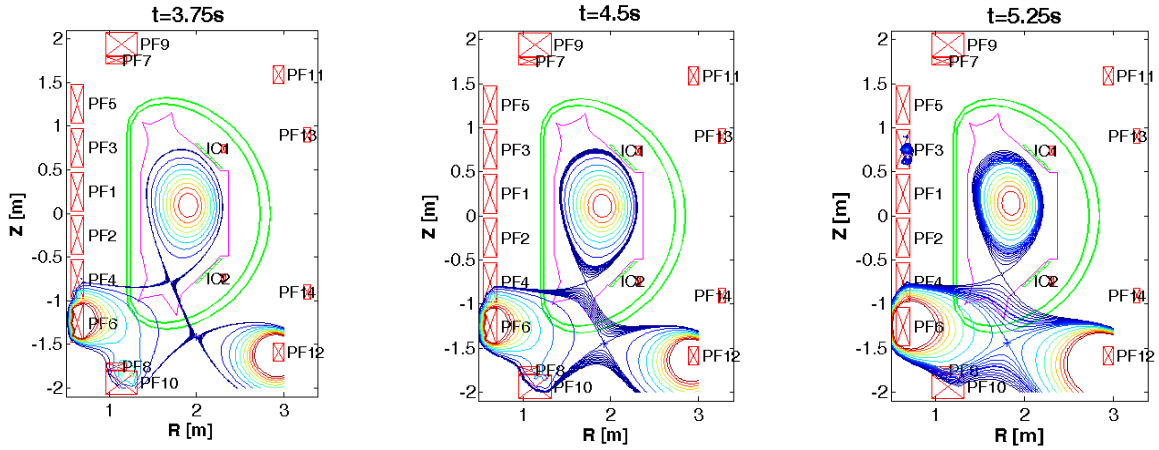

Figure 9. Sequence of EFIT equilibria for ohmic QSF discharge #47660 at 3.75, 4.5 and 5.25s.

In EAST, as previously discussed, the secondary x-point could be moved around and configurations could vary from a SF like to an X-d like configuration. In this preliminary experiment the secondary x-point is moving during the discharge evolution (see Fig.9) forming a configuration with significant distance between the two nulls and a flaring geometry near the plate. Two L-mode discharges with similar input power (~500kW), similar effective charge Z_{eff}~4.5 and electron average density n_e~1.2x$10^{19}m^{-3}$, but with different configurations (the standard divertor SN versus the QSF) will be compared. Core and edge diagnostic used in this study are described elsewhere [12, 33, 34]. In Fig.10. the EFIT reconstructed equilibria for QSF #48971 (at t=4.5s, with β_p=0.76 and l_i=1.28) and SN #47038 (at t=4.5s, with β_p=0.58 and l_i=1.56) discharges are shown. Also the low-divertor Langmuir Probes (LPs) arrays are shown [34]. It should be noted that the experimental SN discussed here shows a contracting geometry near the plate. Experimental magnetic geometry properties for both configurations are compared in Table II. These results confirm the predictions discussed in the previous sections: the presence of a secondary null-point in QSF reduces B_p/B_{tot} in the divertor separatrix region, where B_{tot} is the total magnetic field, and this increases the connection length by ~30% and the flux expansion in the outer SP region by a factor ~4. The experimental QSF magnetic field angle at the outer SP region is below the technological limit discussed here [14], i.e. the magnetic field angle at SPs should be greater than 1°. But, it should be noted that the QSF configuration has been obtained at high q_{95}~8 whilst operating at low q_{95}~3 the magnetic field angle should be >1°. This obtained QSF configuration shows a value PF6 = 8.3kA as the maximum PF coil current during the discharge evolution, well below the limit. The experimental connection length is higher than the predictive one, discussed in section 2, of a factor ~1.5 for both QSF and SN, as expected due to the fact that the experimental I_P is ~45% lower than the simulated one.

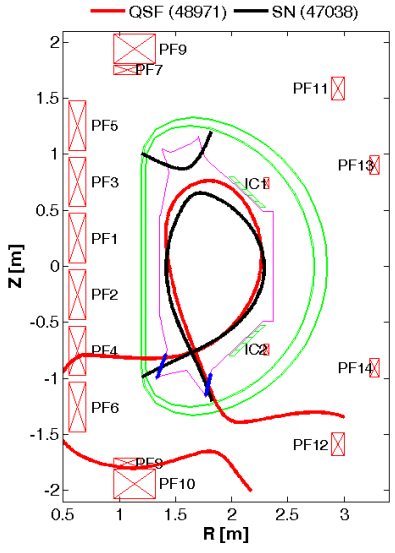

Figure 10. Schematic 2D view of EAST with SN #47039 at t=4.5s (black solid line) and QSF (red solid line) at t=4.5s plasma boundaries. The x-point separation D is = 79cm for the QSF discharge. Also the low-divertor LPs arrays (blue solid points) are shown: inner LI01..15 (from the top to the bottom of the target) and outer LO01…LO20 probes [34].

TABLE II: MAIN MAGNETIC GEOMETRY FOR SN AND QSF DISCHARGES

	QSF, #48971 at t=4.5s	**SN, #47038 at t=4.5s**
SOL Volume [m^3]	0.389	0.260
Connection Length [m]	189.91	144.38
Magnetic flux expansion at outer SP $f_{m,out}$	8.22	2.01
Magnetic field angle at outer SP α_{out} [deg]	0.33	1.22
Magnetic flux expansion at inner SP $f_{m,in}$	4.71	2.34
Magnetic field angle at inner SP α_{in} [deg]	0.90	1.29

Time evolution of main plasma quantities for SN and QSF discharge are shown in Fig.11: plasma current I_P, line avarage electron density n_e, additional heating P_{HEAT} (Lower Hybrid (LH) and NBI power respectively for #47038 and #48971), total radiated power P_{RAD} from Bolometer diagnostic, q_{95} and elongation κ. Up to 3 sec the plasma configuration is limiter, then a transition phase from limiter to QSF configuration has been obtained as programmed. At ~4.3 sec the QSF shape becomes stable, i.e. no variation on elongation or q_{95} is present. Preliminary spatio-temporal profiles of the ion saturation current density j_{SAT} for both QSF and SN discharges are shown in Fig. 12. Only inner and outer low-divertor LPs arrays are considered in this study. The error bar for LPs measurements are ±10% [34]. In SN discharge #47038 both inner and outer LPs are quite active all the time. On the contrary, once the QSF shape becomes stable, the peak of j_{SAT} on the outer target is observed to drastically drop indicating a possible heat flux reduction. In order to investigate this experimental observation, interpreative 2D edge simulations with TECXY code have been performed for the two discharge at t=4.5sec and the simulated heat load has been compared to the one measured by Infrared (IR) camera diagnostic [33].

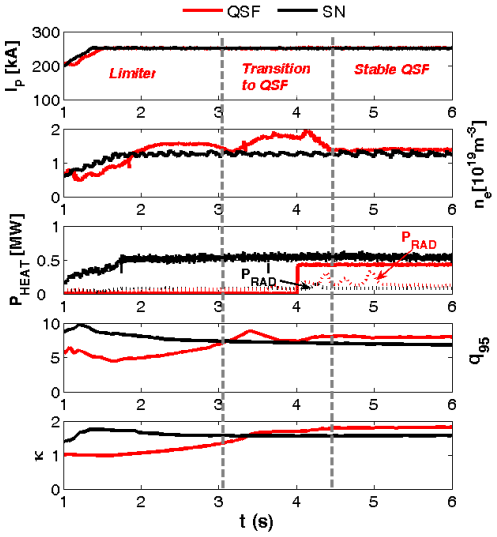

Figure 11. Time evolution of main plasma quantities for SN (#47038) and QSF discharge (#48971): plasma current I_P, interferometer line average electron density n_e, additional heating P_{HEAT} (LH and NBI power respectively for discharges #47038 and #48971), total radiated power P_{RAD} from Bolometer diagnostic, q_{95} and elongation κ.

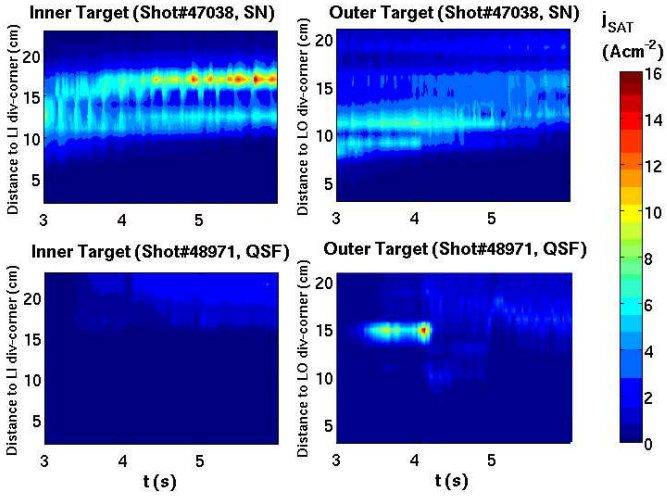

Figure 12. Spatio-temporal profiles of ion saturation current density j_{SAT} for SN (#47038) and QSF discharge (#48971). Once QSF shape becomes stable, the peak of j_{SAT} is observed to drastically drop indicating a possible heat flux reduction.

The experimental input power to the SOL used in the simulations have been: P_{SOL} = 431.7kW in the SN and P_{SOL} = 414.5kW for the QSF case (a slightly higher radiation has been observed in QSF discharge). Electron density at the outer mid-plane (OMP) separatrix $n_{e,sep}$ has been taken from reflectometer diagnostic to be $6x10^{18}m^{-3}$ for SN and $3.34x10^{18}m^{-3}$ for QSF discharge. No impurity has been considered. In Fig.13 the power density at the lower outer target is shown versus the distance along the target and compared to the the simulated one, where zero is considered to be the position of the strike point. Since TECXY assumes a target perpendicular to the flux lines, all the data shown have been corrected taking into account the tilt angle of the target. The simulated peak heat flux does seem to be in good agreement with the experimental data pointing out the heat flux reduction for the QSF configuration, that we

consider to be related only to the higher flux expansion at this low electron density as discussed in section 3. A strong mitigation of the peak deposition power is expected to appear at higher density, as combination of the flux expansion, which dominates at low density, and of the enhanced dissipation processes, which dominates at the higher densities.

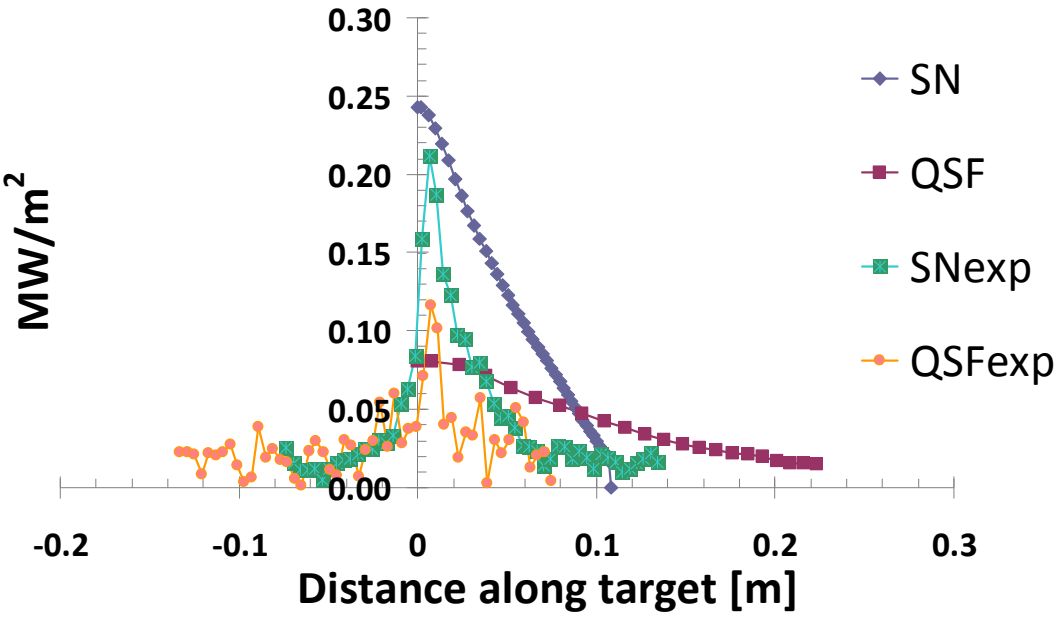

Figure 13. IR measured (labelled as "SNexp" and "QSFexp")and simulated power density (labelled as "SN" and "QSF") by TECXY at the lower outer target.

5. Conclusions

It has been experimentally demonstrated that a quasi-SF configuration may be obtained in EAST tokamak. First experiments have been devoted to investigate the configuration with significant distance between the two nulls and a flaring geometry near the target plates: an increase of the connection length by ~30% and the flux expansion in the outer SP region by a factor ~4 with respect the SN has been obtained, confirming the predictions of the optimization study set up by CREATE-NL tools in combination with FIXFREE and EFIT equilibrium codes. It has been observed that in L-mode discharge the peak of ion saturation current density in LPs drops once the QSF shape becames stable compared to a SN case, that could indicate an heat flux reduction. In order to verify this experimental observation, preliminary interpretative 2D edge simulations have been performed using the TEXCY code showing a good agreement between the IR measured and simulated peak heat load that highlight a reduction for this quantity in QSF case, mainly due to the increase of the flux expansion with respect the SN. These first experiments also indicate that the plasma current could be increased by a futher optimization of the configutation and that it is possible to play around with the distance of the two x-points in order to change the topological features of the configuration. In addition, predictive 2D edge similations highlighted that the heat flux mitigation apparently improves at highest densities, and should be particularly evident with high additional heating power, since a stronger absolute drop of the loads has to develop for the same mitigation factor. In the coming EAST experiments the already upgrade of ISOFLUX control system will allow to control the exact position of secondary x-point. This will permit to increase the additional heating power and to easily vary some of the features of

the topological configuration, i.e. moving from a flaring to a contracting geometry near the target plates.

Acknowledgments

The authors gratefully acknowledge the helpful discussions with Dr D. D. Ryutov, Dr E. Kolemen, Prof. S. Mahajan, Dr. H. Reimerdes and Dr. P. Micozzi. This work has been carried out within the framework of the EUROfusion Consortium and has received funding from the European Union's Horizon 2020 research and innovation programme under grant agreement number 633053. The views and opinions expressed herein do not necessarily reflect those of the European Commission. In addition, this work was partly supported by Italian MIUR under PRIN Grant No. 2010SPS9B3, by the National Magnetic Confinement Fusion Research Program of China under Grant No 2014GB103000, the National Natural Science Foundation of China under Grant No. 11305216.

References

[1] LOARTE A., et al., Nucl. Fusion **47** (2007) S203

[2] EICH T., et al, Phys. Rev. Lett. **107** (2011) 215001

[3] KOTSCHENREUTHER M., et al., Phys. Plasmas **14** (2007) 72502

[4] VALANJU P.M., et al, Phys. Plasmas **16** (2009) 056110

[5] RYUTOV D.D., Phys. Plasmas **14** (2007) 064502

[6] RYUTOV D.D., et al., Phys. Plasmas **15** (2008) 092501

[7] RYUTOV D.D., et al., Phys. Scr. **89** (2014) 88002

[8] PIRAS F., et al., Plasma Phys. Control. Fusion **51** (2009) 055009

[9] SOUKHANOVSKII V.A., et al., J. Nucl. Mater. **415** (2011) S365–8

[10] ALLEN S., et al., Proc. 24th Int. Conf. on Fusion Energy (San Diego, CA, 2012) and www-naweb.iaea.org/napc/physics/FEC/FEC2012/html/presentations/801 PD12.pdf

[11] PITTS R.A., et al. J. Nucl. Mat. **290-293** (2001) 940

[12] WAN Y., et al., Overview progress and future plan of EAST Project Proc. 21th Int. Conf. on Fusion Energy 2006 (Chengdu, China 2006) (Vienna: IAEA) CD-ROM file OV/1-1 and www-naweb.iaea.org/napc/physics/fec/ fec2006/html/index.htm

[13] XIAO B.J., et al., Fusion Eng. Des. **83** (2008) 181

[14] RYUTOV D.D., et al., Plasma Phys. Control. Fusion **54** (2012) 124050

[15] VIJVERS W.A., et al., Nucl. Fusion **54** (2014) 023009

[16] KOTSCHENREUTHER M., et al., Phys. Plasmas **20** (2013) 102507

[17] KOTSCHENREUTHER M., et al., presented at 25th FEC-IAEA conference, S. Petersburg, Russia Confederation (2014), IC/P6-43

[18] MATTEI, M., et al., "CREATE-NL+: a Robust Control-Oriented Free Boundary Dynamic Plasma Equilibrium Solver", presented at 28th Symposium on Fusion Technology, San Sebastian, Spain (2014), P1.036

[19] LAO L.L., et al., Nucl. Fusion **25** (1985) 1611

[20] ALLADIO F., CRISANTI F., Nucl. Fusion **26** (1986) 1143

[21] GUO Y., et al., Plasma Phys. Control. Fusion **54** (2012) 085022

[22] ALBANESE R., et al., Plasma Phys. Control. Fusion **56** (2014) 035008

[23] AMBROSINO R., et al., Nucl. Fusion **54** (2014) 123008

[24] CHEN, S.L., Nucl. Fusion **55** (2015) 013010

[25] ALBANESE, R. and VILLONE, F., Nucl. Fusion **38** (1998) 723

[26] VILLONE, F., et al., Plasma Phys. Control. Fusion **54**, (2012) 085003

[27] ZAGÓRSKI R., GERHAUSER H., Physica Scripta **70** (2004) 173

[28] WANG, L., et al., Nucl. Fusion **54**, 114002 (2014)

[29] PERICOLI RIDOLFINI V., et al., Fus. Eng. Des. **88** (2013) 1677

[30] SIMONINI R., et al., Contrib. Plasma Phys. **34** (1994) 368

[31] WAN B., et al., presented at 25th FEC-IAEA conference, S. Petersburg, Russia Confederation (2014), OV/3-3

[32] XIAO, B.J., et al., Fusion Eng. Des **87 (**2012) 1887

[33] GAO, U., et al., Plasma Sci. Technol. **16** (2014) 93

[34] WANG, L., et al., Nucl. Fusion **52**, 063024 (2012)